Eur. J. Mineral., 38, 263–280, 2026
https://doi.org/10.5194/ejm-38-263-2026

European Journal of Mineralogy
Open Access

Retrograde crystallization of clay minerals in metamorphic rocks linked to fluid circulation related to fault activity

Isabel Abad[1], **Matías Reolid**[1], **Juan Jiménez-Millán**[1], **and Fernando Nieto**[2]

[1]Departamento de Geología and CEACTEMA, Universidad de Jaén, Campus Las Lagunillas, 23071, Jaén, España
[2]Departamento de Mineralogía y Petrología, Universidad de Granada, Fuentenueva s/n, 18002, Granada, España

Correspondence: Isabel Abad (miabad@ujaen.es)

Received: 4 September 2025 – Revised: 9 March 2026 – Accepted: 6 April 2026 – Published: 11 May 2026

Abstract. The study of two outcrops of schists in the Padul Fault area has allowed us to corroborate the enrichment in clay minerals in the fault zone. In the case of the dark schist outcrop, the fault rocks show a reduction in mineral diversity with aluminosilicates, characteristics of the regional metamorphism losing and showing an enrichment in quartz and kaolin-group minerals. In the calc-schists, there is a clear presence of chlorite in the fault rocks, which is practically absent in the fresh rocks, as well as R1 illite/smectite and smectite. The geochemical characterization also showed differences between fresh and fault rocks, more evident in the dark schists than in the calc-schists, with an increase in SiO_2 but a significant decrease in Al_2O_3, Fe_2O_3, and MgO in the fault rocks with respect to the protolith. The presence of authigenic chlorite in the fault rocks from the calc-schists allowed for the application of semi-empirical thermometric methods for the fault rocks giving predominant temperatures < 225 °C. All these data are consistent with the circulation of low-temperature fluids along the fault zone that interact with the rocks, promoting clay mineral formation. Such was also the findings in a previous study focused on the predominant rocks of the Padul Fault area, which are dolostones, affected by the dynamics of this fault. Interestingly, the circulation of fluids promoted by the existence of the Padul Fault has not been restricted to the fault rocks, given that some of these clay minerals (kaolinite and smectite) are also present in the fluid-accessible zones of the metamorphic protolith. These data highlight the importance of faults in the retrograde mineralization processes of metamorphic rocks.

1 Introduction

It is known that the southern Iberian Peninsula is a tectonically active area as a result of the convergence of the Eurasian and the Nubian plates. A main feature of this geotectonic context is the existence of a good number of active faults (e.g., Sanz de Galdeano, 1990, 2012; Galindo-Zaldívar et al., 2003, 2015; Stich et al., 2024). Some of them accommodate the extension in a predominantly NW–SE strike, as is the case for the Padul Fault (Ruiz et al., 2003; Galindo-Zaldívar et al., 2007; Hürtgen et al., 2013; Rodríguez-Peces et al., 2014; Gil et al., 2017).

In fact, the Padul Fault is the best exposed active normal fault of the central Betics (Betic Cordillera, Spain) and the principal active fault of this area (Alfaro et al., 2001). But the absence of instrumental or historical records of seismic events suggests that the fault is now unlocked and that its activity occurs, at least partially, by creep, reducing the possibility of large seismogenic events (Gil et al., 2017). Abad et al. (2022) identified authigenic clay minerals in the dolomitic fault rocks (mainly chlorite but also talc and smectite) as a consequence of fluid–rock interaction processes under temperatures < 220 °C. These results are consistent with the geodetic characterization of this fault by Gil et al. (2017), demonstrating that the genesis of minerals with extremely

low friction coefficients and preferential orientation in the fault plane and surrounding rocks can promote weakening mechanisms at shallow crustal levels that contribute to the creep over the seismic stick-slip (Wintsch et al., 1995; Collettini et al., 2009; Smeraglia et al., 2017).

Most of the rocks affected by the Padul Fault are Triassic dolostones of the Trevenque Unit of the Alpujárride Complex affected by low-grade metamorphism (Sanz de Galdeano and López-Garrido, 1999; Sanz de Galdeano and Alfaro, 2004). The Alpujárride Complex also includes Palaeozoic metapelitic sequences (mainly schists) below the Triassic carbonate sequences (e.g., Aldaya et al., 1979; Tubía et al., 1992; Sanz de Galdeano and López-Garrido, 2003). In this sense, in the extreme of the NW segment of this 13 km long fault outcrop, rocks corresponding to lower stratigraphic and/or tectonic positions – that is, Palaeozoic dark schists of the Guindalera Klippe and Permian calc-schists of the Trevenque Unit – are the ones studied here. These outcrops give us the opportunity of deepening our knowledge of these lithologies (fresh protolith and fault rocks), not only for understanding the mineralogical and geochemical changes that they have undergone as a consequence of a dynamic metamorphism during the development of the extensional fault zone under a low-temperature environment, but also for contributing to a more global vision of the chemical changes affecting the upper dolostones that have previously been studied. For this purpose, we have compared the results of this research with the data corresponding to the fault areas where mainly dolostones are affected (Abad et al., 2022) to (1) advance the knowledge of the mineral reactions, chemical changes, and textural changes promoted by the mechanical behavior of the Padul Fault and the fluid–rock interactions as a consequence of this and (2) to evaluate possible differences according to various lithologies. In a broader context, we have correlated the clay mineral patterns with others described in faults around the world according to the review by Xu et al. (2023) and the clay minerals anomalies that they defined.

2 Geological setting and materials

The study outcrops are located in the footwall block of the Padul Fault, corresponding to the Sierra del Manar, a relief composed mainly of rocks of the Alpujárride Complex, one of the metamorphic complexes that constitutes the Internal Zone of the Betic Cordillera subject to major tectonism and large displacements during the early Miocene (e.g., Sanz de Galdeano, 1990; Braga et al., 2003) (Fig. 1a).

The Padul Fault trends NW–SE with a variable dip to the SW ranging from 60–65° to < 20° and is made up of a northwestern segment that is 5.3 km long (close to Padul village) and a southeastern segment that is 7 km long (close to the Dúrcal and Nigüelas villages) connected by a 1.5 km long relay fault. Despite the fact that the displacements along the fault plane are mainly normal, there is a slight to moderate left lateral component (Gil et al., 2017).

The fault separates the highest reliefs of Sierra Nevada (footwall block) from the Padul graben at the southeastern border of the Granada Basin (e.g., Sanz de Galdeano, 1976; Sanz de Galdeano and Alfaro, 2004), resulting in a spectacular mountain front, which is the Sierra del Manar, constituted mainly by Upper Triassic dolostones with low-grade metamorphism that constitute the upper part of the stratigraphic succession of the Trevenque Unit (Sanz de Galdeano and López-Garrido, 1999, 2003). Below the Triassic dolostones there are Permian calc-schists of the Trevenque Unit outcropping in smaller areas. Locally, in the Sierra del Manar, there are dark schists and calc-schists of the Guindalera Klippe (Permian to Lower Triassic) that correspond to lower terms of the Guajares Unit (Sanz de Galdeano and López-Garrido, 2003).

The genesis of the Padul Fault is certainly later than the early Tortonian, since at the top of the Sierra del Manar, there are marine sediments of the Quéntar Formation (lower Tortonian) and the Pinos Genil Formation (also called Block Formation, upper Tortonian) (see also Braga et al., 2003). During all this time, the fault has been working, lifting, and exhuming materials that have been eroding, giving rise to fossil (hanging) alluvial fans and other current ones (see also Alfaro et al., 2001). According to Stich et al. (2024), the Padul Fault, as well as other faults surrounding the Granada Basin, would be rooted between 10 and 12 km deep (consistent with Morales et al., 1997). Gil et al. (2017) calculate a movement of 0.5 mm yr^{-1}, currently with a significant horizontal component. Surrounding the principal fault there is a dense joint system as well as many normal conjugate faults with a NW–SE strike in the immediate vicinity of the principal fault (Alfaro et al., 2001; Rudersdorf et al., 2011), which constitute the fault zone.

For this research, fault rocks and their respective protoliths were collected from two sites: La Romera and La Raja (Fig. 1b). In the La Romera outcrop (37°02′51.80″ N, 3°38′34.60″ W), a total of 10 samples were obtained along a cross-section composed of Palaeozoic dark schists of the Guindalera klippes (Aldaya et al., 1979) from 55 m to the fault plane in the footwall block. These rocks are recorded in the NW end of the Sierra del Manar relief and correspond to the Guajares Unit (Simancas and Campos, 1993; Alonso-Chaves and Orozco, 1998; Sanz de Galdeano and López-Garrido, 2003), which overthrusts the Trevenque Unit (Sanz de Galdeano, 1990). In the La Raja outcrop (37°02′24.87″ N, 3°37′51.22″ W), a total of 15 samples were taken along a cross-section composed of Permian calc-schist levels from the base of the carbonate formation of the Trevenque Unit (see also Sanz de Galdeano and López-Garrido, 1999) from 60 m to the fault plane and in the footwall block. These calc-schists are interbedded with more carbonated rocks (commonly dolostones), which are all affected by the fault (Fig. 2a). The dark schists and calc-schists are easily rec-

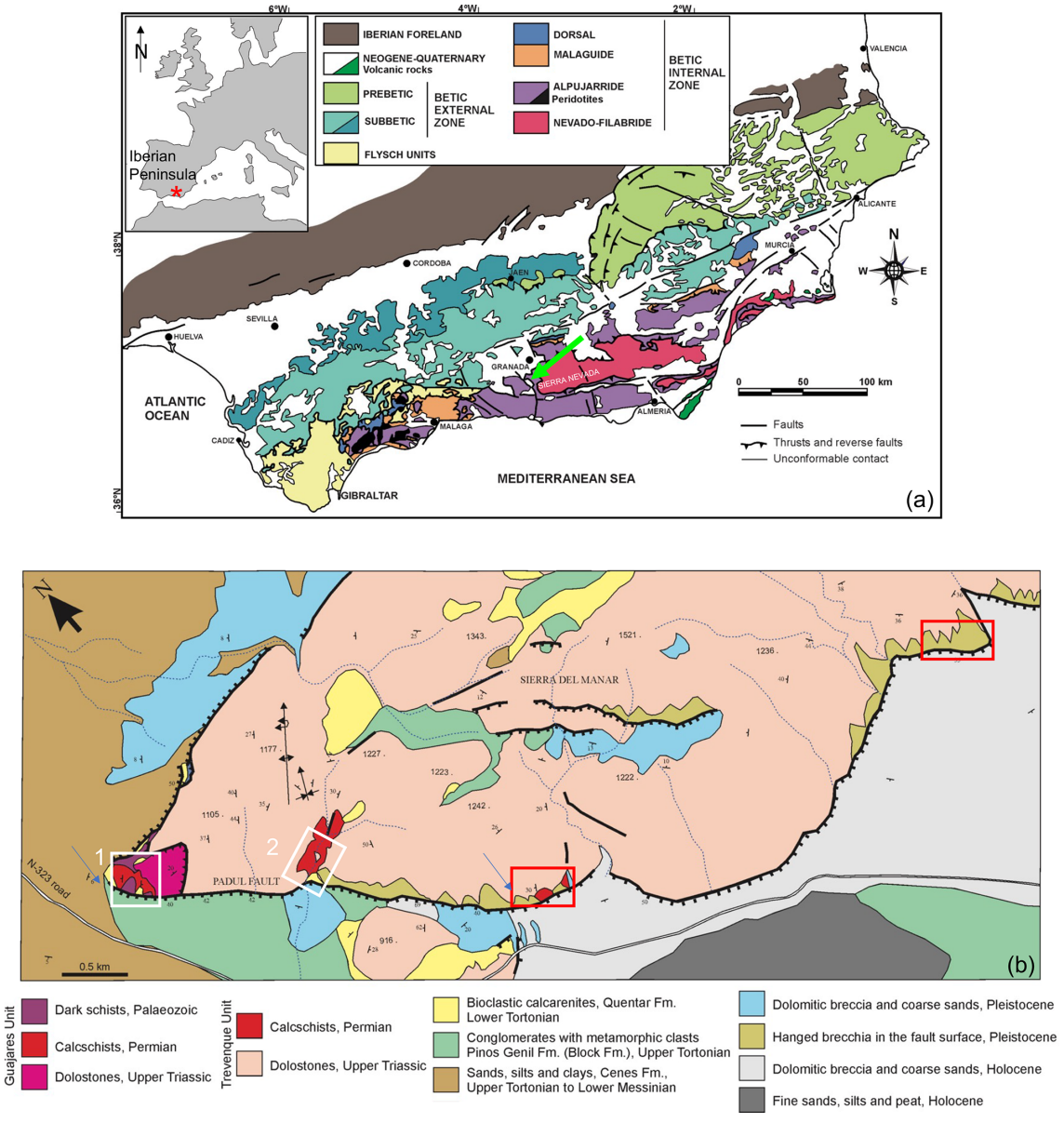

Figure 1. **(a)** Geological map of the study area with an indication of the location of the Padul Fault (green arrow) in the Internal Zone (Alpujárride Complex) of the Betic Cordillera (modified from Fig. 3 in Sanz de Galdeano, 2022). **(b)** Detailed geological map of the Padul Fault in the south of the Granada Basin with an approximated indication of the studied outcrops (white rectangles, 1: La Romera; 2: La Raja; red rectangles: outcrops studied in Abad et al., 2022). Modified from Abad et al. (2022).

ognizable in the outcrops by their clear foliated texture (Fig. 2b). In addition, the dark schists usually have a golden appearance in hand samples due to the abundance of micas. In the fault plane, they show a breccia texture (Fig. 2c).

3 Methods

Whole-rock analyses of the major elements of selected samples from the protoliths and fault rocks were carried out in order to compare the variation in the chemical composition of different samples. A PANalytical Zetium wavelength dispersive X-ray fluorescence (XRF) spectrometer was used with a maximum power of 4 kW, equipped with an X-ray tube with an Rh anode. Samples were prepared as beads with a Philips Pearlx3. Trace elements were analyzed in the same samples using a NexION 300D inductively coupled plasma-mass spectrometer (ICP-MS) after HNO_3 + HF digestion of 100 mg of sample powder in a Teflon-lined vessel at 180 °C and 200 p.s.i. for 30 min, evaporation to dryness, and subsequent dissolution in 100 mL of 4 vol % HNO_3, with both techniques taking place at the Centro de Instrumentación Científica (CIC), University of Granada, Spain.

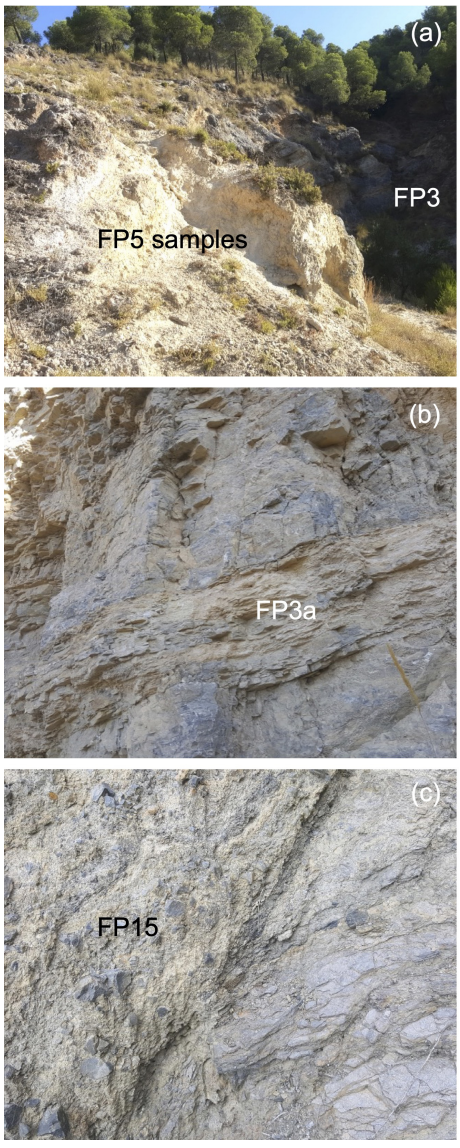

Figure 2. **(a)** View of the La Raja outcrop, fault rocks in the sunny area (FP-5 samples), and the fresh calc-schists in the shade (FP-3 samples); **(b)** appearance of the calc-schists sampled in the La Raja outcrop with a foliated texture that is absent in the surrounding carbonated rocks; and **(c)** dark schists next to the fault with the characteristic breccia texture on the left (La Romera outcrop).

X-ray diffraction (XRD) data were obtained from unoriented powders and oriented aggregates prepared by sedimentation on glass slides after crushing to a fine powder and disaggregation in an ultrasonic bath. Ethylene glycol and dimethyl-sulfoxide treatments were carried out to allow the identification of expandable minerals. XRD analysis was performed using a PANalytical empyrean diffractometer operating with Bragg–Brentano geometry (CuKα radiation, 45 kV, 40 mA) equipped with an X'Celerator solid-state linear detector and θ/θ goniometer with a virtual step increment of 0.01° 2θ and a counting time of 10 s per step at the Centro de Instrumentación Científico-Técnica (CICT) of the University of Jaén (Spain). The powder samples were scanned between 4 and 64° 2θ, while for the oriented aggregates (included the ones treated with ethylene-glycol, EG, and dimethyl-sulfoxide, DMSO), the scanning was between 4 and 32° 2θ.

Following XRD, thin sections ($\sim$ 30 µm thick) prepared with epoxy resin and mounted in glass slides were oriented approximately normal to the dominant planar fabric and characterized under magnifying glass and a petrographic microscope at various magnifications. Carbon-coated polished thin sections were examined by scanning electron microscopy (SEM), using atomic number contrast backscattered electron (BSE) imaging and energy dispersive X-ray spectroscopy (EDX) analysis to obtain textural and qualitative chemical identification of minerals. These observations were carried out using a Carl Zeiss Merlin Gemini II SEM with a resolution of 0.8 nm and five detectors (one in-lens detector for high resolution) at the CICT (University of Jaén).

Chlorite thermometry was applied to the calc-schists (fresh and fault rocks) based on chemical data obtained by electron microprobe (EPMA) and transmission electron microscopy (TEM) analysis. EPMA analyses of chlorites were obtained using wavelength-dispersive spectroscopy (WDS) on a JEOL JXA-iSP100 super probe at the CIC (University of Granada). The instrument was set at an accelerating voltage of 20 kV, with a beam current of 5 nA and an electron beam diameter of $<$ 1 µm. Data were reduced using the PHI-RHO-Z XPP method (Pouchou and Pichoir, 1991), and the standards used were albite, orthoclase, periclase, wollastonite, baryte, and synthetic oxides (Al_2O_3, Fe_2O_3, Cr_2O_3, and $MnTiO_3$). For the TEM analysis, samples were prepared using a Cu grid surface coated in a perforated formvar resin from a dispersion of finely ground sample particles in alcohol. The monomineralic character of each grain was checked by its electron diffraction pattern, confirming the existence of a single network and, therefore, a single crystalline phase. The TEM study was carried out at the CIC (University of Granada) with a Thermo Fisher Scientific TALOS F200X microscope operated at 200 kV, equipped with a super-X system (four energy dispersion X-ray EDX detectors) and with a point-to-point resolution of 0.12 nm in the TEM mode and 0.19 nm in the scanning transmission electron microscopy (STEM) mode. The nanoscale chemical characterization of chlorites and the compositional maps (X-ray elemental maps) were carried out in STEM mode using the High-Angle Annular Dark Field (HAADF) detector. This system allows for the integration of all the individual spectra of each pixel of the map to produce a spectra sum corresponding to selected polygons of the chemical maps. In this way, homogeneous areas can be chosen for quantitative analysis, after the map has been recorded. For quantitative micro-analyses, EDX data were corrected by the thin-film method (Cliff and Lorimer, 1975). The K factors for the transformation of intensity ratios to concentration were determined using the following as standards: anor-

thite, anorthoclase, apatite, augite, biotite, chromite, hemimorphite, microcline, muscovite, rhodonite, scapolite, osumilite, and spessartine.

Semi-empirical thermometric methods (Bourdelle et al., 2013; Lanari et al., 2014; Inoue et al., 2018) were applied in analyzed chlorites under the conditions previously indicated via the spreadsheet from Verdecchia et al. (2019). The choice of these chlorite thermometers was guided by the compositional range of the studied chlorites and by the temperature and pressure range of calibration of these geothermometers (Bourdelle, $T < 350\,°C$ and $P < 4$ kbar; Lanari, 100–500 °C and 1–20 kbar; and Inoue, $T < 400\,°C$). In addition, Fe, which is present in low quantities here (< 1.20 atoms per formula unit, apfu hereafter), was regarded as Fe^{2+} for the calculation of the initial formulae. The Bourdelle and Inoue geothermometers are designed to assume all Fe as Fe^{2+}; $Fe^{3+}/Fe^{2+} = 0.4$ was assumed for the Lanari chl1 geothermometer and a pressure of 4 kbar for the Lanari chl2 geothermometer as a compromise to reach a good correspondence with the rest of the proposed geothermometers. The uncertainties in the temperature calculations are approximately $\pm 50\,°C$.

4 Results

4.1 Petrography

4.1.1 Dark schists

The dark schists from the La Romera outcrop (site 1 in Fig. 1b) have a silicate-based mineralogical composition according to the XRD patterns: albite, quartz, K mica, a minor presence of chlorite, and in some of them, also paragonite (Na mica), andalusite, and kaolin-group minerals (Fig. 3a). The SEM study shows the presence of two K micas (muscovite and phengite) and also the presence of garnets (almandine type), staurolite, oxides as ilmenite and rutile, zircon, and apatite (Fig. 4a–b). Moreover, chlorite shows Mg-rich spectra, and K–Na and Na–Ca feldspars have also been identified. These schists show, in general, voids aligned with the foliation, occupied mainly by secondary minerals (chlorite, kaolin-group minerals, and oxides) surrounded by albite (Fig. 4b–c) and also domains at micrometer scale ($< 10\,\mu m$) with smectite (Fig. 4d).

The fault rocks formed from the dark schists show a less diverse mineralogy and a distinctly different texture. The XRD patterns show that these rocks are composed of quartz, mica, kaolin-group minerals, and a minor presence of chlorite (Fig. 3a). The kaolin-group mineral shows a peak at 11.23 Å after DMSO treatment. The SEM study completes this mineralogical characterization, showing three micas – phengite, muscovite, and paragonite – and some oxides (Fig. 5). The garnets, albite, and aluminosilicates as andalusite and staurolite were not identified. Texturally, these rocks are heterometric, with angular clasts of the schists of < 0.5 cm in diameter, immersed within a ground mass composed of very fine grained material (Fig. 5a–d). The clasts are more abundant than the matrix, and the mechanical crushing of the protolith is evident. Some BSE images of these samples show veins and clay-rich matrices composed mostly of densely packed kaolin-group crystals of a few micrometers as subhedral flakes forming book-type aggregates (Fig. 5c–e). These aggregates generate a flow and folded pattern (Fig. 5e).

4.1.2 Calc-schists

Regarding the calc-schists (site 2 in Fig. 1b), the XRD data indicate a mineralogical composition based mainly on calcite and/or dolomite and silicates as mica, minor quartz, and feldspars (Fig. 3b). These rocks have a foliated appearance due to the presence of muscovite and biotite, as it was corroborated under the SEM, which contrast with the surrounding more carbonated rocks (Figs. 2b and 6).

In some of the calc-schists sampled in the fault plane or very close to it, there is an evident presence of chlorite and also a low-intensity peak at 12.44 Å, which after the EG treatment shows a lower intensity at 12.21 Å and a new peak at 16.91 Å. This indicates the presence of an R1 illite/smectite and smectite (Fig. 3b). These fault rocks show a different textural aspect, with a mixture of carbonates (predominant calcite and minor dolomite) and phyllosilicates (chlorite, biotite, and muscovite), more clearly oriented but fragmented and with voids in the surroundings, and minor quartz and feldspars (Fig. 7a). Chlorite usually forms aggregates, mostly together with biotite, with the appearance of intergrowths (Fig. 7b–d).

4.2 Chemical bulk composition

The XRF data of major elements in the dark schists and the fault rocks from this protolith point to a clear increase in SiO_2 in the fault rocks with respect to the schists but also to a significant decrease in Al_2O_3, Fe_2O_3, and MgO (Fig. 8). In the case of SiO_2, the content is < 67 wt % in the protolith and always > 76 wt % in the fault rocks (Table 1). Al_2O_3 content decreases from values close to 20 wt % to values around 8 wt % in the fault rocks and Fe_2O_3 from 8 wt %–3 wt %. In the case of MgO, the decrease is more subtle as the initial content of MgO in the dark schists is close to 2 wt % and in the fault rocks around 0.7 wt %. Other elements, such as Na_2O, K_2O, and TiO_2, also decrease in the fault rocks (Table 1).

In the calc-schists, there is no clear chemical differences between the major elements of the protolith and the fault rocks (Table 1). The content of Al_2O_3 and Fe_2O_3 is very similar, and SiO_2 is slightly lower in the fault rocks (Fig. 8a–b). Nevertheless, in both cases (fresh and fault rocks), two compositional groups can be distinguished on the basis of CaO and MgO contents: rocks with CaO contents between

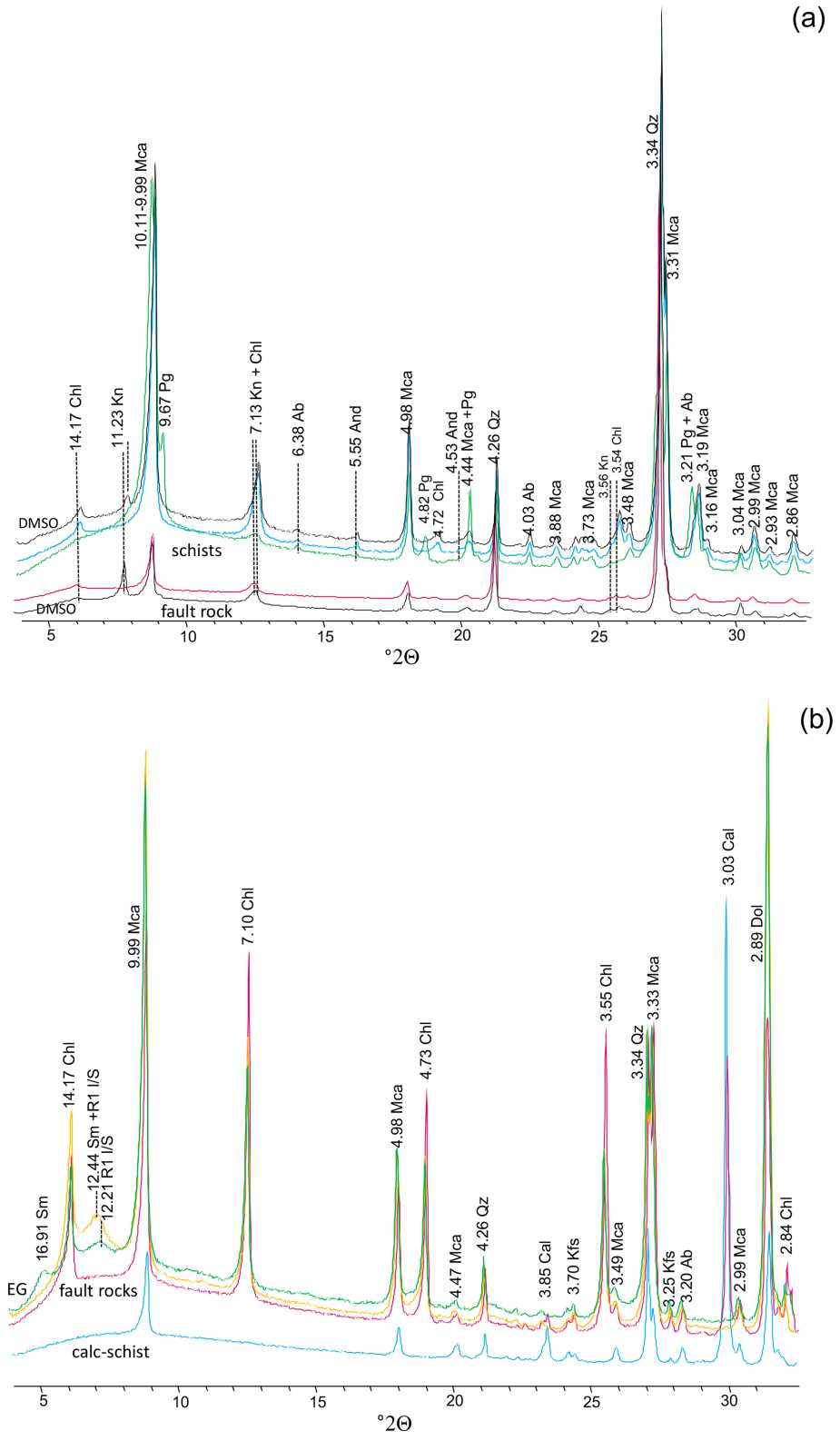

Figure 3. Representative XRD patterns of oriented aggregates of the two lithologies studied: **(a)** dark schists (blue and green) and the corresponding fault rocks in fuchsia; the black profiles correspond to DMSO-treated samples having Kn; **(b)** calc-schists (blue) and the corresponding fault rocks (fuchsia and yellow); the green profile corresponds to the EG-treated sample of the yellow profile one. Numbers indicate d values in Å. Mineral abbreviations according to Warr (2021): Ab, albite; And, andalusite; Cal, Calcite; Chl, chlorite; Dol, dolomite; Kfs, K-feldspars; Kn, kaolin-group mineral; Mca, mica; Qz, quartz; and Pg, paragonite.

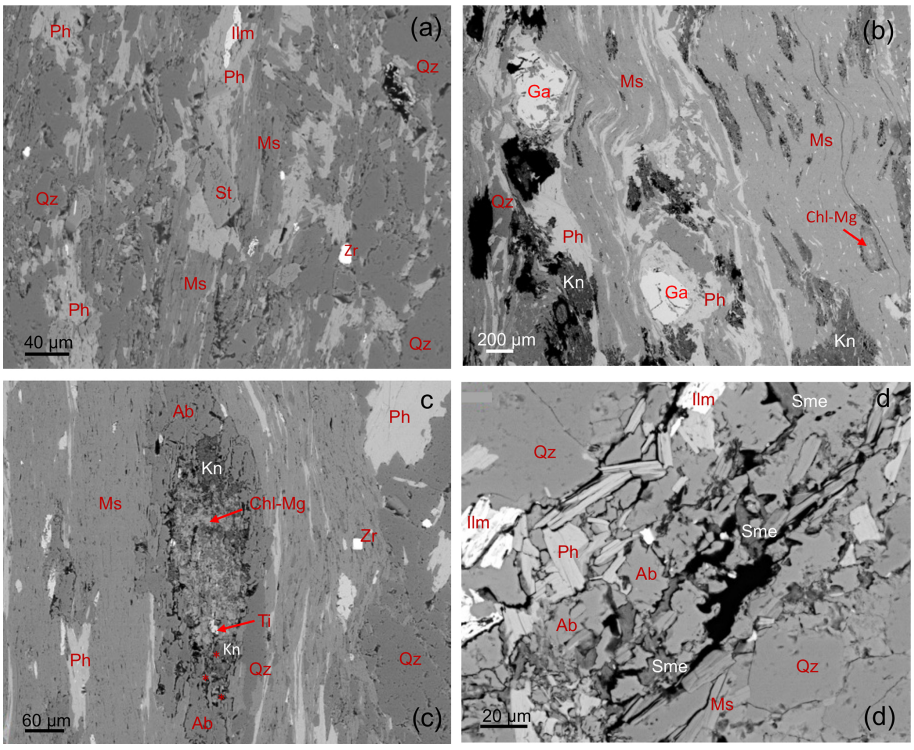

Figure 4. BSE images showing the texture and chemical features of the dark schists: **(a)** detail of alternation of phyllosilicate-rich bands with phengite and muscovite mainly and bands rich in quartz; **(b)** highly foliated phyllosilicate-rich band with micas that wrap garnets and also elongated holes occupied by chlorite and irregular and bigger holes filled by kaolin-group minerals; **(c)** detail of one of the elongated holes showing chlorite in the core but also kaolin-group minerals in the rims and surrounded by albite; and **(d)** quartz-rich domain including feldspars, oxides, micas, and smectite in micrometer gaps. Mineral abbreviations according to Warr (2021): Ab, albite; Chl, chlorite; Ga, garnet; Ilm, ilmenite, Kn, kaolin-group mineral; Ms, muscovite; Ph, phengite; Qz, quartz; Sme, smectite; St, staurolite; and Zr, zircon.

27 wt % and 37 wt % and MgO 5 wt %–7 wt % and rocks with CaO contents between 11 wt % and 24 wt % and higher MgO contents (11 wt %–15 wt %), which have dolomite but not calcite (Fig. 8c).

Trace elements are higher in the dark schists than in the fault rocks (Table 2, see e.g., Li, Cs, Sr, V, Cr, Ni, Cu, Zn, Ga, Nb, Ta, Sn, Pb, Th). However, in calc-schists, as in the major elements, there is no clear chemical differences between the trace elements of protolith and fault rocks, except for an impoverishment in Rb, Sr, Ba, and U and an enrichment in Zn in the fault rocks with respect to the fresh rocks (Table 2).

According to these observations, the enrichment factors (EFs) were calculated for some of the trace elements. The enrichment factor is based on Al normalization and is written as $X_{\mathrm{EF}} = [(X/\mathrm{Al})_{\mathrm{sample}}/(X/\mathrm{Al})_{\mathrm{PAAS}}]$, where X is a specific trace element, and PAAS is the post-Archean average shale compositions of Taylor and McLennan (1985). In practical terms, EFs > 3 represent a detectable enrichment of an element over average crustal concentrations, and EFs > 10 represent a moderate to strong degree of enrichment (Algeo and Tribovillard, 2009). In this case, $\mathrm{Zn_{EF}}$ is > 10 only in one calc-schist but in several fault rocks of this protolith. Pb_{EF} is significant too for these rocks, with values > 3 in fault rocks and even > 10 in some of the protolith samples (Table 2). Regarding the dark schists, $\mathrm{Pb_{EF}}$ is between 3 and 8 in the protolithic rocks and two of the fault rocks (Table 2).

Rare earth elements (REE), normalized to CI carbonaceous chondrite (McDonough and Sun, 1995), of fresh rock (dark schists and calc-schists) and fault rock averages display a similar trend with a very slight Eu anomaly, except for the fault rocks from calc-schists. There is also a higher abundance in light REE (LREE) compared to heavy REE (HREE) for all of them (Fig. 9). However, with respect to the dark schists, fresh calc-schists are slightly richer in HREE and, at the same time, slightly depleted in LREE.

4.3 Chlorite chemistry and thermometry

Semi-empirical thermometry was applied in chlorite-bearing fault rocks of calc-schists (two samples) and in the only fresh calc-schist, with some chlorite, sampled in this location (La Raja outcrop), for comparative purposes. Due to the very occasional presence of chlorite in the fresh calc-schists, it was not possible to locate chlorite grains by EPMA. In the case of the fault calc-schists, where the abundance of chlorite (Figs. 3b and 7b) is more evident, the problem was that

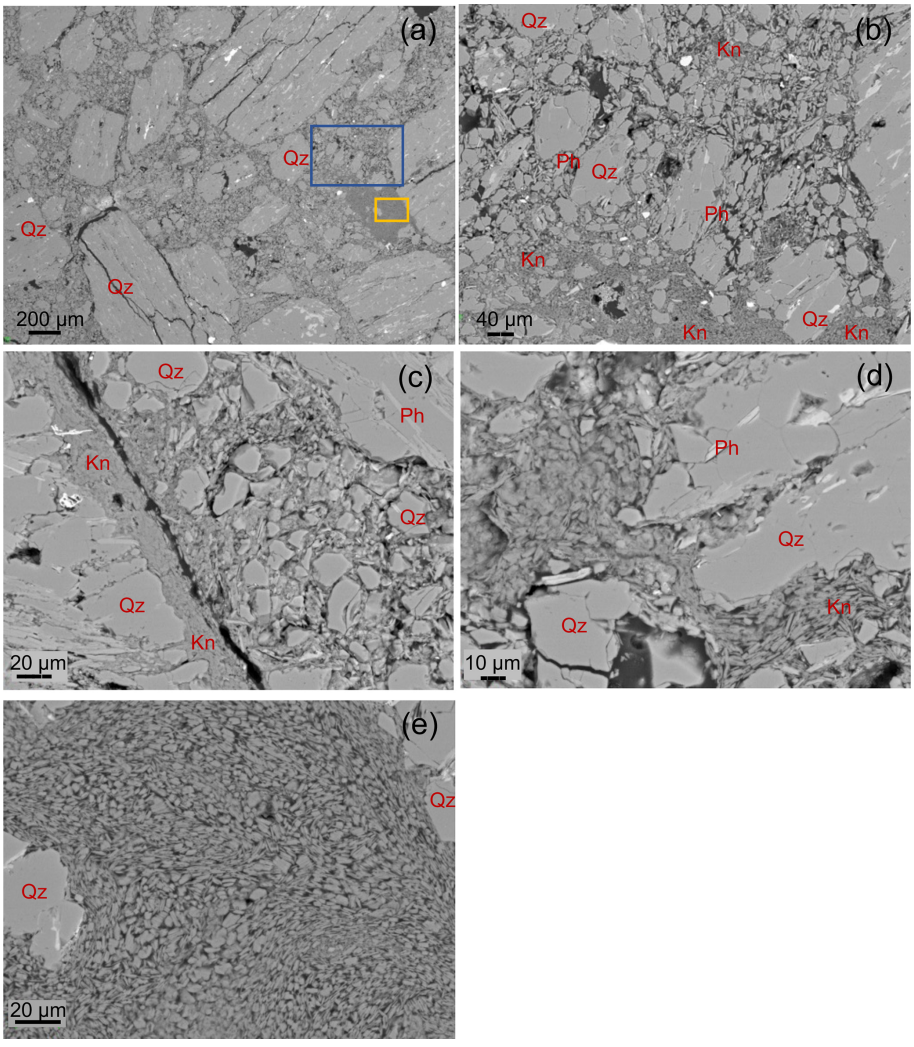

Figure 5. BSE images corresponding to a dark schist taken in the fault plane. **(a)** General view of the fault breccia composed of angular clasts of the schists immersed in a fine-grained matrix, **(b)** enlargement of a detail of **(a)** (blue square) where a predominance of quartz clasts with a minor presence of mica and a matrix mostly composed of kaolin-group minerals are observed, **(c)** vein partially filled by kaolin-group minerals, **(d)** quartz clasts and some mica laths surrounded by a fine-grained matrix which includes kaolin minerals, and **(e)** detail of the matrix (yellow square in Fig. 5a) with kaolin subhedral plates of a few micrometers forming book-type aggregates. Mineral abbreviations according to Warr (2021): Kn, kaolin; Ph, phengite; and Qz, quartz.

chlorite is in most cases intergrown with biotite (Fig. 7c–d). As a consequence, most of the EPMA chlorite analyses show a K content higher than allowed by the geothermometers restrictions due to contamination, with the obtention of only 16 analyses from 8 grains free of K. For this reason, it was decided to obtain microanalysis in the TEM of both type of samples (fresh and faulted calc-schists).

The chlorites of these samples, based on EPMA and TEM results, are Mg rich (clinochlore variety) and also include Al and Fe in the octahedral sites, but in quantities always < 1.6 and < 1.2 apfu, respectively (Tables S1 and S2 in supplementary material). To completely characterize the chlorite chemistry, all the obtained compositions, free of other phyllosilicate contamination, according to the interlayer sum, have been represented in Fig. 10a–b, independently of their applicability or not (due to thermodynamic reasons) to the geothermometers (see below). Chlorites define very similar fields for the two cases, with only narrower and slightly higher ranges for the Mg in the case of chlorites of the protolith.

For thermometry, chlorite analyses were selected according to the criteria related to the sum of interlayer cations and octahedral vacancies given by each of the employed geothermometers. The temperature estimations for these thermometers are rather similar (Table 3). There is a wide range of temperatures for the two lithologies, although the predominant values for the fault rocks, based on the TEM data, are $< 225\,^{\circ}C$ (Fig. 11a) lower than temperatures coming

Table 1. Whole-rock analyses of major elements of Padul Fault samples (oxide wt %. XRF). In brackets is the distance to the fault plane.

Samples	SiO_2	Al_2O_3	Fe_2O_3	MnO	MgO	CaO	Na_2O	K_2O	TiO_2	P_2O_5	LOI	Total
Dark schists												
FP-11 (55 m)	63.11	17.71	7.29	0.08	2.3	0.81	0.94	3.07	0.89	0.2	3.44	99.84
FP12 (50 m)	66.55	14.74	8.09	0.15	1.87	1.68	1.81	1.67	0.86	0.14	2.29	99.85
FP-13 (15 m)	56.39	21.67	8.53	0.08	1.75	0.72	1.49	3.82	1.1	0.2	3.77	99.52
FP-14 (12 m)	57.41	21.65	8.39	0.09	1.88	0.45	1.69	3.64	1.09	0.21	3.3	99.8
Fault rocks												
FP-15a	82.19	8.65	3.37	0.02	0.68	0.33	0.32	1.55	0.65	0.09	2.16	100.01
FP15b	81.92	7.97	2.84	0.05	0.65	0.93	0.26	1.47	0.65	0.1	2.87	99.71
FP15c	83.45	8.31	2.55	0.07	0.59	0.35	0.28	1.52	0.5	0.09	2.16	99.87
FP15d	76.69	8.42	4.4	0.06	1.28	2.57	0.3	1.19	0.59	0.11	4.19	99.8
Calc-schists												
FP-3a (40 m)	15.19	4.97	1.73	0.01	5.1	36.64	0.06	1.75	0.28	0.06	33.81	99.6
FP-3c (55 m)	23.06	7.58	2.39	0.03	5.89	30.26	0.3	2.23	0.34	0.06	27.44	99.58
FP-3d (58 m)	24.55	8.91	3.66	0.03	13.88	17.15	0.05	3.46	0.44	0.11	27.45	99.69
FP-3f (60 m)	29.65	9.99	4.03	0.05	14.39	13.86	0.08	4.17	0.46	0.11	22.89	99.68
FP-3g (58 m)	36.43	11.37	4.73	0.05	11.54	11.79	0.06	4.76	0.49	0.12	18.56	99.9
Fault rocks												
FP-5a	23.26	8,00	3.31	0.05	6.6	27.34	0.54	2.1	0.4	0.08	27.69	99.37
FP-5b	17.52	5.52	2.14	0.02	14.66	23.76	0.04	1.77	0.29	0.1	34.03	99.85
FP-5c	13.66	4.7	1.71	0.01	6.39	36.95	0.07	1.12	0.22	0.06	34.95	99.84
FP-5d	23.52	6.76	2.43	0.04	14.68	19.58	0.05	1.93	0.32	0.07	30.15	99.53
FP-5e	24.55	10.23	4.96	0.02	15.04	15.35	0.47	2.77	0.5	0.11	25.68	99.68
FP-5f	22.45	3.89	1.73	0.02	14.65	22.53	0.05	1.21	0.18	0.08	32.67	99.46

from EPMA (Fig. 11b). This difference is attributed to the smaller crystals analyzed by TEM, which formed under lower-temperature genetic conditions. The chlorites from the fresh calc-schist (TEM data) have a predominant temperature range between 225–275 °C (Fig. 11c). In addition to the represented temperatures in Fig. 11, a significant number of analyses of the two lithologies (blue dashed circle in Fig. 10a) present compositions outside the valid range of applicability of the geothermometers due to their total octahedral populations very close to 6 apfu. This chemical condition, which is characteristic of high-temperature chlorites, does not allow for the quantitative determination of the temperature (Vidal et al., 2016). With increasing temperature, the chemical composition of chlorite becomes progressively less affected (note how isotherms converge in Fig. 10a), rendering the geothermometric application impossible.

5 Discussion

In line with the work of Abad et al. (2022) based on the study of Triassic dolostones of the Alpujárride Complex affected by the Padul Fault, here we have focused on two other outcrops along this fault, affecting different lithologies: dark schists and calc-schists.

5.1 Chemical and mineralogical changes promoted in schists and calc-schists by the development of the fault zone

The rocks affected by a fault usually show, in addition to distinct textural features, a mineral and chemical composition that is different to the protolith, and, in most cases, there is an enrichment of clay minerals (Xu et al., 2023). The clay minerals formed in the fault zone depend on the chemical features of the protolith but also on the external physical and chemical conditions (presence and composition of fluids, temperature, and pressure conditions, among others). A dynamic metamorphism generates fault rocks through crushing, ductile creep, recrystallization, and even neocrystallization.

In this study, we detected that the mechanisms of deformation for the two types of rocks were different, resulting in a predominant cataclastic texture in the faulted dark schist (Fig. 5) and ductile creep in the faulted calc-schist (Fig. 7), and that there is a variability in the mineralogy of both lithologies.

A reduction in the mineral diversity of the dark schists affected by the fault was observed with the presence of quartz, kaolin-group minerals, and micas and the disappearance of albite and regional metamorphic aluminosilicates formed under higher temperatures (such as andalusite, staurolite, and

https://doi.org/10.5194/ejm-38-263-2026

Table 2. Trace elements (ppm, ICP-MS) of Padul Fault samples. EF: enrichment factor.

Samples	Dark schists				Fault rocks (schists)				Calc-schists					Fault rocks (calc-schists)					
	FP 11	FP12	FP13	FP 14	FP 15a	FP15b	FP15c	FP 15d	FP 3a	FP 3c	FP 3d	FP 3f	FP 3g	FP 5a	FP5b	FP5c	FP5d	FP5e	FP5f
Li	39.25	30.73	92.72	80.59	18.3	17.56	21.2	54.01	44.93	78.4	185.63	300.86	307.94	69.81	65.34	59.77	111.77	192.98	80.39
Rb	20.69	80.41	91.51	92.72	65.9	33.47	34.29	41.88	38.13	69.15	91.23	115.23	129.66	49.8	46.01	43.47	57.61	77.82	31.98
Cs	5.77	6.97	10.51	8.97	4.24	2.66	2.6	2.53	2.77	4.64	8.42	14.05	16.58	5.22	4.89	17.03	6.62	9.81	3.72
Be	1.99	1.93	3.45	1.9	1.51	1.36	1.45	1.57	0.86	1.55	1.61	1.78	2.21	1.19	1.46	1.13	1.41	2.05	0.94
Sr	64.9	102.87	97.93	103.17	51.08	43.92	47.95	108.09	476.74	883.37	546.47	431.67	199.97	408.02	138.33	121.58	120.96	154.03	154.77
Ba	136.72	370.97	493.47	559.01	267.34	165.83	119.06	153.39	349.18	167.42	245.77	201.22	224.46	181.38	172.31	91.96	137.8	189.79	76.72
Sc	5.56	13.6	11.93	10.78	5.8	3.95	2.51	6.05	4.2	7.8	9.3	10.46	12.18	6.82	5.52	4.67	6.21	11.03	3.3
V	146.38	89.47	197.25	165.89	55.2	48.98	46.65	53.26	94.48	62.29	73.18	79.95	91.21	52.91	54.45	43.08	56.26	93.95	34.88
Cr	91.82	71.29	127.02	114.83	43.29	36.53	32.06	37.3	30.63	32.76	46.85	52.64	61.41	41.36	26.63	18.38	28.76	57.71	13.08
Co	16.15	13.5	18.8	16.11	6.84	7.95	11.17	7.44	5.26	3.83	5.18	12.06	15.77	10.21	2.86	3.48	8.39	6.48	5.87
Ni	39.58	23.97	59.19	46.92	16.27	15	19.25	16.05	28.69	25.27	28.73	27.4	60.17	26.95	25.25	40.82	30.73	50.52	27.18
Cu	17.45	11.08	35.02	29.14	10.77	7.04	21.62	10.34	10.14	17.06	23.72	24.53	31.34	13.82	12.7	13.27	11.37	29.94	10.66
Zn	105.22	57.59	108.64	104.64	44.97	24.56	26.52	36.49	462.37	40.14	58.86	83.32	67.36	31.23	209.66	291.58	158.63	1315.92	236.03
Ga	22.2	16.32	28.87	25.96	10.36	9.07	9.06	9.78	5.23	10.89	12.47	13.68	16.01	9.36	8.52	6.63	9.48	14.33	5.59
Y	10.02	21.61	6.87	5.34	9.47	10.02	5.1	11.45	7	14.74	14.53	15.66	11.11	15.16	11.36	13.77	8.45	9.88	8.59
Nb	15.81	17.22	20.37	18.24	11.1	9.7	8.18	10.04	5.35	7	8.87	9.37	10.14	0.77	5.68	4.73	6.39	10.7	3.93
Ta	1.11	1.18	2.48	1.4	0.82	0.75	0.67	0.77	0.4	0.69	0.78	0.83	0.9	0	0.56	0.45	1.28	1.1	0.44
Zr	5.64	2.75	26.26	20.91	15.04	23.87	28.06	26.65	32.08	33.46	50.13	53.81	61.94	5.17	29.83	20.55	34.27	57.92	19.06
Hf	0	0	0.75	0.33	0.16	0.47	0.6	0.53	0.74	0.98	1.51	1.57	1.85	0	0.85	0.61	1.06	1.76	0.5
Mo	0.79	0.49	0.86	1	0.55	1.26	1.49	0.71	9.28	1.59	3.78	1.81	4.34	67.22	6.5	4.44	7.27	12.27	5.23
Sn	4.57	3.04	5.61	5.41	2.34	1.84	2.11	1.49	0.23	1.71	1.81	1.99	2.42	0.66	0.93	0.97	1.36	2.19	0.65
Tl	0.56	0.42	1.06	0.9	0.38	0.3	0.29	0.28	1.6	0.42	0.75	1.23	3.06	1.01	1.24	7.45	3.15	3.37	2.04
Pb	23.32	24.02	31.19	27.07	13.59	8.55	5.07	5.64	155.67	10.67	44.33	18.54	23.2	15.27	9.27	15.33	19	24.08	12.5
U	1.6	1.83	2.46	1.99	1.45	0.97	0.86	1.72	3.91	4.48	5.45	5.64	11.24	1.6	3.18	1.96	3.06	4.5	2.84
Th	8.92	10.07	10.14	7.32	7.82	5.47	2.66	7.77	4.1	5.77	6.23	6.21	7.4	4.27	4.37	3.6	5.09	8.31	2.99
La	25.27	33.16	26.11	17.56	27.84	20.62	10.98	30.82	8.56	16.86	16.17	22.21	23.79	20.32	14.92	14.37	10.75	14.7	15
Ce	56.49	67.45	36.62	27.3	63.11	46.86	19.62	58.8	17.56	34.54	34.64	46.64	48.26	43.07	50.43	20.8	29.81	40.03	32.19
Pr	6.36	7.71	6.65	4.38	6.26	4.91	2.54	7.23	2.06	4.25	4.43	5.5	5.58	4.85	3.79	3.51	2.51	3.86	3.71
Nd	24.46	28.7	25.79	16.88	23.13	18.63	9.74	27.63	8.03	16.83	17.64	21.22	20.75	18.93	15.06	14.11	10.05	14.71	14.19
Sm	4.7	5.64	5.07	3.33	4.4	3.64	1.86	5.35	1.6	3.75	3.74	4.34	3.82	3.94	3.2	2.94	2.06	2.91	2.63
Eu	1.1	1.27	1.08	0.75	0.95	0.89	0.49	1.31	0.43	1.03	0.68	0.87	0.87	1.18	0.9	0.79	0.56	0.58	1.1
Gd	3.056	4.57	3.11	2.152	3.011	2.5	1.1	3.72	0.982	2.63	2.6	3.04	2.48	3.004	2.23	2.06	1.26	1.82	1.51
Tb	0.37	0.7	0.38	0.27	0.35	0.32	0.12	0.48	0.14	0.4	0.41	0.46	0.41	0.44	0.3	0.32	0.22	0.27	0.21
Dy	2.03	3.83	1.81	1.39	1.84	1.81	0.84	2.34	1.06	2.46	2.52	2.79	2.12	2.54	1.9	2.08	1.28	1.72	1.37
Ho	0.38	0.71	0.29	0.22	0.33	0.35	0.19	0.39	0.26	0.51	0.52	0.55	0.4	0.51	0.4	0.47	0.3	0.39	0.31
Er	1.05	1.65	0.83	0.68	0.88	0.93	0.6	1.01	0.79	1.41	1.5	1.54	1.17	987	1.11	1.21	0.86	1.1	0.87
Tm	0.16	0.22	0.13	0.11	0.13	0.14	0.1	0.15	0.13	0.21	0.22	0.22	0.17	0.19	0.17	0.18	0.13	0.17	0.13
Yb	0.99	1.3	0.79	0.68	0.8	0.9	0.63	0.9	0.82	1.23	1.42	1.42	1.15	1.08	1.03	1.06	0.91	1.06	0.84
Lu	0.14	0.18	0.11	0.09	0.11	0.12	0.09	0.13	0.12	0.18	0.22	0.21	0.17	0.16	0.15	0.16	0.14	0.15	0.12
Zn_{EF}	1.14	0.75	0.96	0.93	1.00	0.59	0.61	0.83	17.82	1.01	2.27	1.60	1.13	0.75	7.28	11.88	4.50	24.64	11.62
Pb_{EF}	4.19	5.18	4.58	3.98	5.00	7.18	1.94	2.13	99.61	4.48	15.82	5.90	6.49	6.07	5.34	10.37	8.94	7.49	10.22

Table 3. Summary of temperatures in chlorites with semi-empirical methods.

	Sample	Range (°C)	Average (°C)	*n*
Bourdelle et al. (2013)		95–345	172± 70	25
Lanari et al. (2014) Chl (1)	Fault rocks from calc-schist	165–288	230± 44	8
Lanari et al. (2014) Chl (2)	(TEM data)	145–285	208± 48	8
Inoue et al. (2018)		70–445	208± 118	20
Bourdelle et al. (2013)		96–259	198± 62	16
Lanari et al. (2014) Chl (1)	Fault rocks from calc-schist	213–290	259± 23	12
Lanari et al. (2014) Chl (2)	(EPMA data)	161–271	236± 31	12
Inoue et al. (2018)		68–268	209± 86	8
Bourdelle et al. (2013)		75–258	192± 63	13
Lanari et al. (2014) Chl (1)	Fresh calc-schist	223–245	279± 31	7
Lanari et al. (2014) Chl (2)	(TEM data)	207–297	262± 31	7
Inoue et al. (2018)		38–406	276± 116	8

garnets). According to the patterns of clay minerals in fault zones presented by Xu et al. (2023), based on the types of the clay minerals present in single or multiple combinations, in the dark schists, the enrichment on quartz and kaolin minerals in the fault rocks fits with the felsic anomaly category, specifically the kaolinite type anomaly. This kind of category is usually developed from protoliths which include rock-forming minerals such as feldspars and micas, whose alteration can produce kaolinite (Xu et al., 2023). The higher-temperature fabric of the dark schists was overprinted by a fault breccia composed of angular clasts of the schists (Fig. 5), increasing their permeability. Through these paths, the circulation of low-temperature fluids probably produced a leaching of the parent material with the dissolution of mineral phases such as albite and even andalusite, contributing, under the new conditions, to the crystallization of kaolin minerals. According to Jiménez-Millán et al. (2007), the transformation of andalusite to kaolinite can be direct in a strongly altered area. A remarkable aspect of the BSE images is the presence of subhedral flakes of authigenic kaolin mineral grown in intergranular pores. The apparent orientation of these crystals suggests a syntectonic origin and a ductile creep (Fig. 5e). This observation, together with the angular clasts of schists mainly formed by quartz and micas in the fault breccia, suggests that the fault registered first brittle and later ductile deformation.

Interestingly, kaolin minerals (and other low-temperature clay minerals, such as smectite) are not restricted to the fault rocks, but they are also present in filling voids aligned with the foliation of the protolith rock (Fig. 4b–d), even in the parent rocks sampled as far as possible from the fault. From the well-known petrography of the dark schists of the Alpujárride Complex (e.g., Aldaya et al., 1979, and references therein; Abad et al., 2003), the kaolin group is not a rock-forming mineral of these rocks, consistent with their formation temperature, which at least reaches the biotite isograd. In fact, phases that are characteristic of low and medium grades of metamorphism, as staurolite, garnet, and andalusite, are present in the studied protolith samples (Figs. 3a and 4). Therefore, the circulation of fluids promoted by the fault must not have been restricted to the obvious fault rock, given that a kaolin mineral is also present, together with smectite, in the fluid-accessible zones of the protolith at distances of at least 55 m. Surrounding the principal fault surface, there is a dense joint system with abundant normal conjugate faults (see also Alfaro et al., 2001; Rudersdorf et al., 2011), which favored the fluid circulation from the Tortonian to the present in deeper parts of the Padul Fault zone, now exhumed. Moreover, the highly fractured dolostones of the Trevenque Unit do not constitute a barrier to fluid circulation. This finding highlights the importance of faults in the retrograde low-temperature mineralization processes of metamorphic rocks, described by Nieto et al. (2005) as retrograde diagenesis.

The calc-schists show the opposite behavior to the dark schists, with greater mineral diversity in the fault rocks than in the protolith. In these rocks, the more distinctive feature is the significant presence of chlorite, which is very scarce in the calc-schists far from the fault zone (Fig. 3b). Texturally, the chlorite is observed next to biotite from the protolith. This relationship was also observed in Abad et al. (2022) in the fault rocks of the dolostone outcrops studied in the Padul Fault zone, where a clear genetic link between both phases facilitated by the structural and chemical similarities was established, using high-resolution TEM. In addition, R1 illite/smectite and smectite were also detected in these fault rocks, contributing to the enrichment in clay minerals in the fault area. According to Xu et al. (2023) and their discussion of anomalous clay patterns found in faults, this case fits with the mafic anomaly category – the chlorite type anomaly. This includes many potential processes for the chlorite genesis, but based on the mineralogical and textural information of the studied rocks, in this case, chlorite probably formed by decomposition of biotite, as previously described in Abad et al. (2022), where it was observed that biotitic packets in-

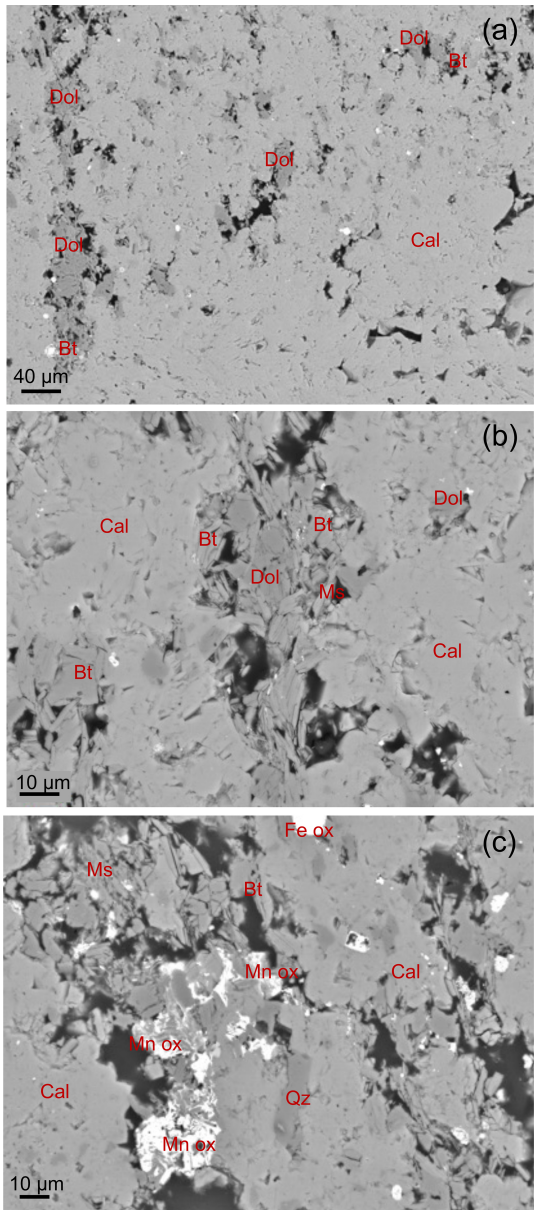

Figure 6. BSE images of the fresh calc-schists: **(a)**–**(b)** View of the calc-schist with a predominance of calcite but with domains of silicates with biotite and muscovite and scattered grains of dolomite; **(c)** presence of oxide (Fe and Mn) quartz grains and micas surrounded by calcite crystals. Mineral abbreviations according to Warr (2021): Bt, biotite; Cal, calcite; Dol, dolomite; Fe ox, Fe oxide; Mn ox, Mn oxide; Ms, muscovite; and Qz, quartz.

cluded 14 Å layers and packets with several layers of 10 Å, alternating with packets of several layers of 14 Å or 24 Å, suggesting a layer-by-layer transformation from parent biotite to chlorite product, facilitated by structural and chemical similarities (see Fig. 8 from Abad et al., 2022). This kind of topotactic replacement of biotite by chlorite is a frequent reaction, previously described in low-grade metamorphic contexts (Jiang and Peacor, 1994; Barrenechea et al., 2000) and also in hydrothermal systems (Jiménez-Millán et al., 2008; Airaghi et al., 2020). Here, the BSE images with chlorites show them finely intergrown with biotite (Fig. 7c–d), and their analyses at micrometric scale (EPMA) mostly show K, confirming the intimate relationship between both of them.

The careful analyses of the data from XRF and ICP-MS show undoubted changes among the rocks studied, which corroborated the fluid-related alterations, in this case, with clear trends in each of the studied lithologies. Moreover, the changes are apparently more evident in the dark schists than in the calc-schists, both in terms of major and trace elements. Specifically, the fault rocks in the dark schists are richer in SiO_2 but depleted in Al_2O_3, Fe_2O_3, and MgO with respect to the fresh dark schists, which can justify in a low-T environment the increase in quartz and even in kaolin minerals as they have a higher proportion of SiO_2 than the metamorphic silicate minerals of the fresh dark schists.

In the case of calc-schists, the formation of chlorite from biotite does not require significant chemical changes, beyond the loss of K. Smectite and illite/smectite are typical products of argillic alteration in hydrothermal environments, at intermediate pH and temperatures lower than 160 °C (Fulignati, 2020). They are the result of the alteration effect of fluids on felsic minerals, as feldspars and/or micas. There is also an impoverishment in trace elements in the fault rocks related to the loss of elements that are soluble under oxidizing conditions. In any case, in a fault which is more than 13 km long, there must be preferential zones of fluid circulation, hence the diversity in trace contents among the samples.

5.2 Connections with the low-temperature processes affecting dolostones of the Padul Fault area

In the dolostones affected by the Padul Fault, Abad et al. (2022) described the genesis of chlorite, talc, and smectite, with the presence also of illitic micas and kaolinite in the dolomitic fault rocks (see Figs. 4 and 11 in Abad et al., 2022). The application of thermometry to chlorites located in the fault plane gave temperatures within the range of 140–220 °C (see Fig. 7 in Abad et al., 2022). In the present study, the temperatures obtained from the application of chlorite thermometry (Bourdelle et al., 2013; Lanari et al., 2014; Inoue et al., 2018) in the calc-schists from the fault plane (La Raja outcrop) show a broad range of conditions, although predominant values are < 225 °C (Fig. 10c). That is, these are similar to some of the temperatures established in dolostones affected by the Padul Fault, where Abad et al. (2022) interpreted them as typical of pervasive hydrothermal fluid upwelling from deep sources. These fluids circulated along the fault plane but also migrated laterally through the permeable fault rocks and conjugate fault system, promoting changes in geochemistry and mineralogy; the process is more evident next to the main fault plane than at a certain distance,

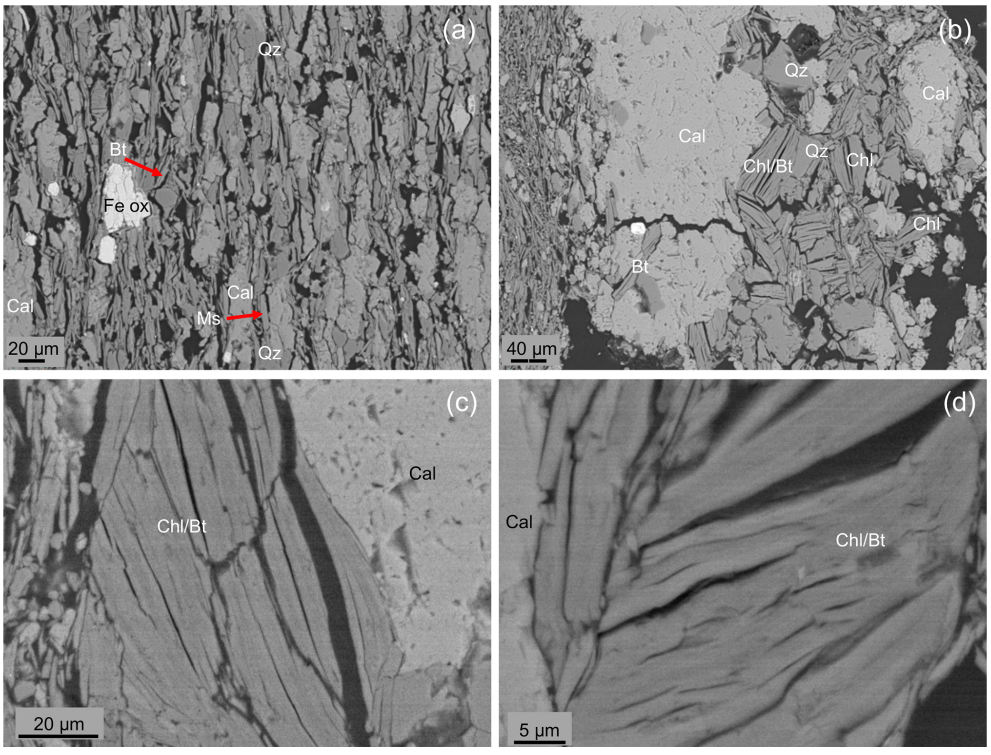

Figure 7. BSE images corresponding to calc-schists from the fault plane: **(a)–(b)** Calc-schist with a major presence of micas but also of quartz and the novel presence of chlorite-forming aggregates; **(c–d)** detail of chlorite aggregates, where the lighter grey zones correspond to biotite and the darker zones to chlorite with a small peak of K in their spectra. Mineral abbreviations according to Warr (2021): Bt, biotite; Chl, chlorite; Cal, calcite; Fe ox, Fe oxide; Ms, muscovite; and Qz, quartz.

also due to the temperature, which would be higher along the main fault planes, contributing to dissolution processes. Both lithologies, calc-schists and dolostones, belong to the Trevenque Unit being the calc-schists stratigraphically below the dolostones. The fact that the fluids upwelled from deep sources is consistent with the wider range of temperatures obtained from the fault calc-schist chlorites reaching values around 300 °C (Figs. 10a and 11a). With respect to the temperatures corresponding to the fresh calc-schists, a more restricted range has been determined using the geothermometers (Figs. 10a and 11c), but all of them have maximum temperatures of application, limited by the condition of a minimum number of octahedral vacancies in the chlorite (Vidal et al., 2016). A significant number of the obtained analyses are outside this condition (area delimited by the blue dotted line in Fig. 10a). In conclusion, the fresh calc-schists contain chlorites crystallized in most cases at temperatures above 225 °C (Figs. 10a and 11c), which is consistent with the conditions of the previously described regional low-grade metamorphism.

The Padul Fault, as other faults surrounding Sierra Nevada, originated during the late Tortonian (see Braga et al., 2003). In the Sierra del Manar, which constitutes the footwall block, there are Tortonian materials (Quéntar Formation and Pinos Genil Formation) outcropping between 1200–1400 m that are located at < 800 m in the graben (hanging-wall block). This means that fluids have circulated along the fault and adjacent areas, especially in the highly fractured dolomites, during the last 7 Ma (see the International Chronostratigraphic Chart; Cohen et al., 2013). According to Stich et al. (2024), the Padul Fault would be entrenched between 10 and 12 km depth, which, according to the average geothermal gradient of 25–30 °C km^{-1}, results in a fluid temperature around 250–300 °C at deeper parts of the fault. The geothermal gradient in Sierra Nevada would be higher than average values (Muñoz-Cemillán et al., 2025), surely stronger during the late Miocene, as expressed by the exceptional concentration of magmatic and metallogenetic episodes of the eastern Betic Internal Zone sector (de Larouzière et al., 1988). These data are congruent with those here obtained from chlorite thermometry and those from Abad et al. (2022). Fission track analyses (Johnson, 1997) and phases of alluvial fan deposition (Braga et al., 2003) confirm that Sierra Nevada underwent a fast uplift during the Pliocene. Therefore, mineralogical and geochemical changes observed in the fault rocks and surroundings were produced during a long time period (from late Miocene to the present) at different depths in rocks now exhumed, for which the coexistence of minerals crystallized at contrasting temperatures is highly expectable. The compositional trend of chlorites in

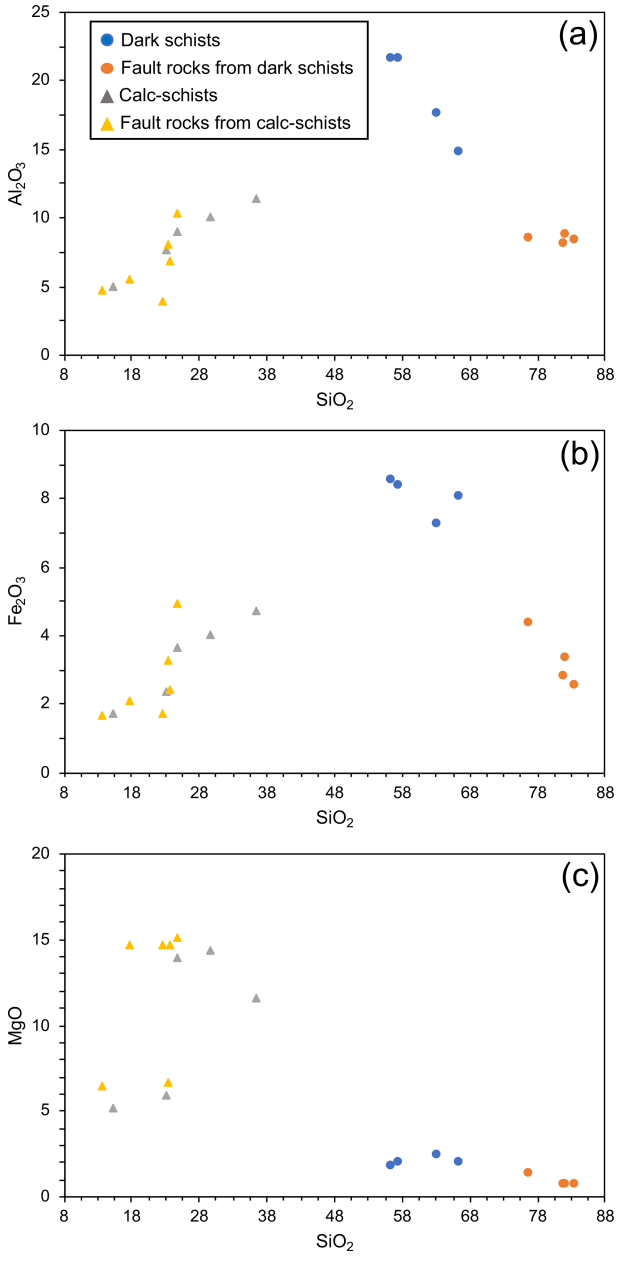

Figure 8. Major element binary diagrams based on X-ray fluorescence data showing chemical differences between the protolith (schists and calc-schists) and respective fault rocks: **(a)** SiO_2 vs. Al_2O_3, **(b)** SiO_2 vs. Fe_2O_3, and **(c)** SiO_2 vs. MgO.

Fig. 10a is compatible with a continuous change of temperature affecting the same composition of the system (Bourdelle, 2021), that is, constant chemistry of the rock and the altering fluids.

A notable aspect of the Triassic dolostones described by Abad et al. (2022) was the presence of Zn with $Zn_{EF} > 10$ in the fault rocks. This was attributed to the high solubility of Zn in hydrothermal systems and the presence of F–Pb–Zn mineral deposits, some of which have been extracted, in the Triassic carbonate sequence of the Alpujárride Complex (Martín et al., 1987). Similarly, in the faulted calc-schists, the Zn content is significant in some, with EF > 10 (Table 2), allowing the effects of Zn-rich hydrothermal fluid circulation, previously proposed by Abad et al. (2022), to be extended to the faulted calc-schists.

The fluid–rock interaction processes along the fault zone are the primary means of clay mineral formation. Regardless of the predominant lithology (dolostones, dark schists, and calc-schist) of the outcrops studied in the Padul Fault, in all cases an enrichment in clay minerals has been detected with proximity to the fault core, that is, in the fault rocks, even if the enrichment in clay minerals is more evident in the calc-schists and dolostones than in the dark schists. As indicated in Abad et al. (2022), the intense cataclasis during the fault activity increases the permeability of the surrounding rock mass, facilitating fluid circulation in the fault zone. Therefore, the fault zone would act as a domain driving mobilized fluids from a deep source. In any case, the clay minerals described here are only stable under low temperatures (< 300 °C). In our studied case, the two main authigenic clay minerals are the kaolin type in the dark schists and chlorite in the calc-schists, as well as the minor presence of smectite and R1 illite/smectite in the fault rocks from calc-schists. Given the stability field of the kaolin mineral, its growth is estimated to occur at < 200 °C, the same as the R1 illite/smectite and smectite, authigenic minerals also present in the dolostones and probably formed during a later stage of circulation of fluids, related to a final step of the hydrothermal activity in the fault. In the case of the dolomitic fault rocks, these terminal fluids promoted calcite mineralization processes that implied the closing of fluid pathways and a reduction in the permeability of the fault rocks.

Finally, the data obtained from the two studied outcrops in relation to the presence of authigenic clay minerals in the fault rocks support the conclusions established in previous work (Abad et al., 2022). The presence of these minerals with very low friction coefficients, such as chlorite and smectite in or next to the fault plane, even in quantities < 3 wt % (Smeraglia et al., 2017), can be a key factor in the behavior of active faults, contributing to the weakening mechanisms at shallow crustal levels with the dissipation of elastic strain energy, particularly in the specific case of the Padul Fault, which promotes aseismic deformation, consistent with the geodetic data from previous research (Gil et al., 2017).

6 Conclusions

The mineralogical data obtained from the fault rocks formed from dark schists and calc-schists affected by the Padul Fault point to processes that favored the enrichment in clay minerals when comparing with the protoliths. The clay minerals described here are only stable under low temperatures (< 300 °C): kaolin minerals in the fault rocks from dark

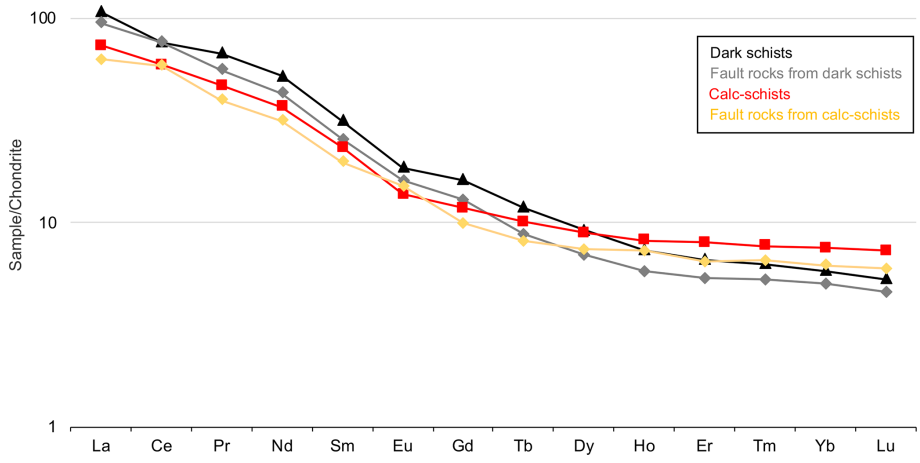

Figure 9. Chondrite normalized REE patterns obtained from the REE average corresponding to each type of sample (see legend).

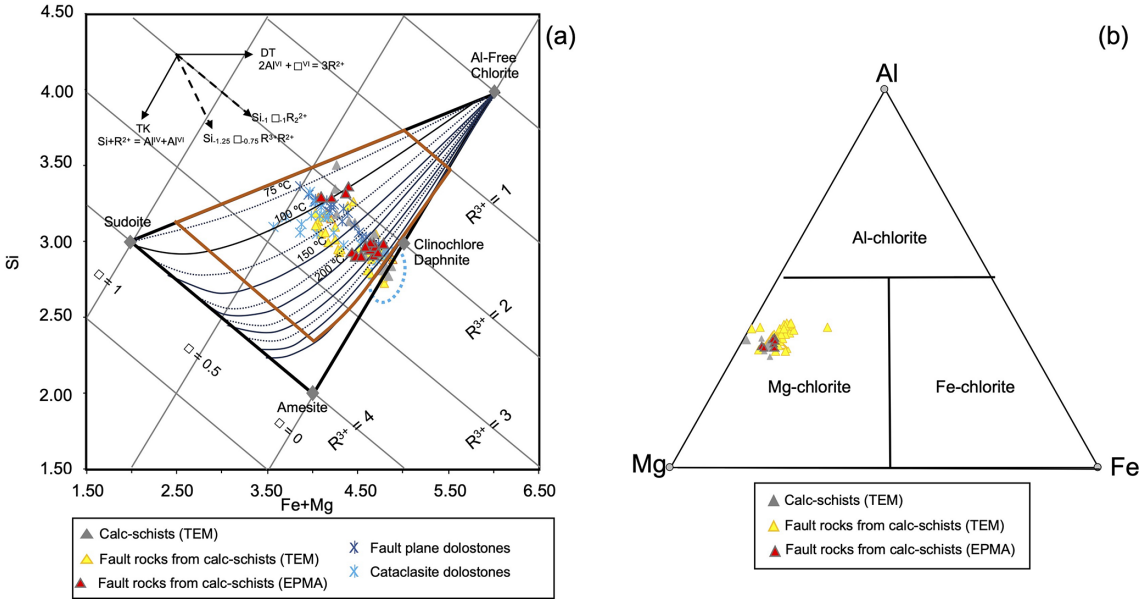

Figure 10. **(a)** Chemical composition of chlorites, normalized to $O_{10}(OH)_8$, from calc-schists studied here and dolostones (from Abad et al., 2022) plotted in the $R2^+$–Si diagram of Wiewiora and Weiss (1990) with the isotherms added by Bourdelle and Cathelineau (2015). The dashed blue line area includes analyses not considered for the temperature calculations due to their higher octahedral sums than the ones accepted by the geothermometric methods. **(b)** Chlorites from calc-schists plotted in an Al–Mg–Fe triangular compositional diagram.

schists and chlorite as well as the minor presence of smectite and R1 illite/smectite in the fault rocks from calc-schists. Specifically, in the case of chlorite, the temperatures obtained were predominantly < 225 °C for the fault rocks and > 225 °C for the fresh calc-schists. The geochemical characterization also shows changes among the rocks studied, which suggested fluid-related alterations promoted by the development of the fault zone not only restricted to the fault rocks, given that minerals such as the kaolin type and smectite are present in the fluid-accessible zones of the protolith. This work highlights the relevance of faults in the retrograde mineralization processes of metamorphic rocks. The results of this research are consistent with the observations made in dolomitic fault rocks, which are the predominant rocks along the Padul Fault, supporting the conclusions established in a previous study and highlighting the role of clays favoring aseismic deformation.

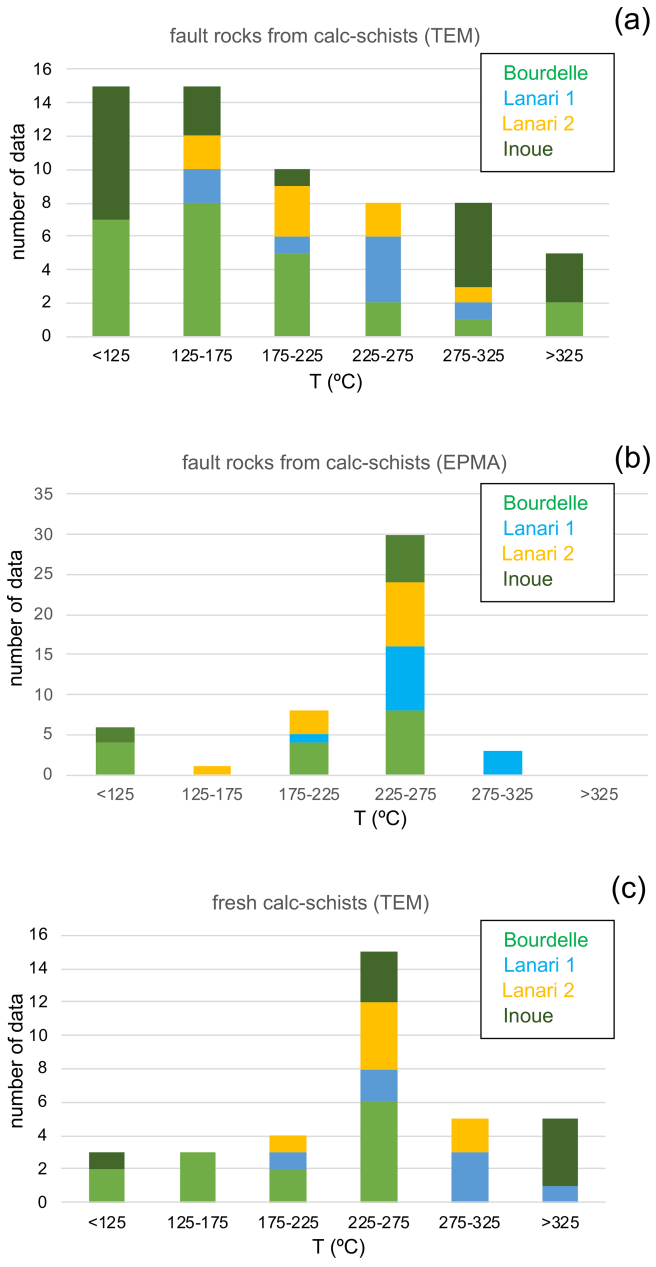

Figure 11. Geothermometric data obtained from the chemical analyses of the chlorites. **(a)** Fault rocks of calc-schists (TEM data), **(b)** fault rocks of calc-schists (EPMA data), and **(c)** fresh calc-schists (TEM data).

Data availability. All relevant data are displayed in the article, and additional data are available upon request from the corresponding author.

Supplement. The supplement related to this article is available online at https://doi.org/10.5194/ejm-38-263-2026-supplement.

Author contributions. I.A. and M.R. conducted field observations and sampling. I.A. and F.N. interpreted the X-ray diffractograms. I.A., M.R., and J.J.M. interpreted the geochemical analyses. I.A., J.J.M., and F.N. performed microscopic observations (SEM and TEM; mineralogical, textural, and chemical analyses; and chlorite geothermometry). All authors discussed the analytical results and prepared the paper (original draft and review).

Competing interests. The contact author has declared that none of the authors has any competing interests.

Disclaimer. Publisher's note: Copernicus Publications remains neutral with regard to jurisdictional claims made in the text, published maps, institutional affiliations, or any other geographical representation in this paper. The authors bear the ultimate responsibility for providing appropriate place names. Views expressed in the text are those of the authors and do not necessarily reflect the views of the publisher.

Acknowledgements. We acknowledge the technical and human support provided by the CICT of Universidad de Jaén (UJA, MINECO, Junta de Andalucía, FEDER). Access to the HAADF Thermo Fisher Scientific TALOS F200X microscope was facilitated by the Centro de Instrumentación Científica of the Universidad de Granada. We are thankful to the Associate Editor Martine Buatier, Javier Cuadros, and the anonymous reviewer for their constructive review comments and suggestions.

Financial support. This research was supported by the PGC2018-094573-BI00 project of MCIU-AEIFEDER and the research groups of Junta de Andalucía RNM-325 and RNM-200.

Review statement. This paper was edited by Martine Buatier and reviewed by Javier Cuadros and one anonymous referee.

References

Abad, I., Nieto, F., Peacor, D. R., and Velilla, N.: Prograde and retrograde diagenetic and metamorphic evolution in metapelitic rocks of Sierra Espuña (Spain), Clay Miner., 38, 1–23, https://doi.org/10.1180/0009855033810074, 2003.

Abad, I., Nieto, F., Reolid, M., and Jiménez-Millán, J.: Evidence of phyllosilicate alteration processes and clay mineral neoformation promoted by hydrothermal fluids in the Padul Fault area (Betic Cordillera, SE Spain), Appl. Clay Sci., 230, 106669, https://doi.org/10.1016/j.clay.2022.106669, 2022.

Airaghi, L., Dubacq, B., Verlaguet, A., Bourdelle, F., Bellahsen, N., and Gloter, A.: From static alteration to mylonitization: a nano- to micrometric study of chloritization in granitoids with implications for equilibrium and percolation length scales, Contrib. Mineral. Petrol., 175, 108, https://doi.org/10.1007/s00410-020-01749-2, 2020.

Aldaya, F., García-Dueñas, V., and Navarro-Vila, F.: Los Mantos Alpujárrides del tercio central de las Cordilleras Béticas. Ensayo de correlación tectónica de los Alpujárrides, Acta Geol. Hisp., 14, 154–166, 1979.

Alfaro, P., Galindo-Zaldivar, J., Jabaloy, A., López-Garrido, A. C., and Sanz de Galdeano, C.: Evidence for the activitly and paleosismicity of the Padul fault (Betic Cordillera, southern Spain), Acta Geol. Hisp., 36, 283–295, 2001.

Algeo, T. J. and Tribovillard, N.: Environmental analysis of paleoceanographic systems based on molybdenum–uranium covariation. Chem. Geol., 268, 211–225, https://doi.org/10.1016/j.chemgeo.2009.09.001, 2009.

Alonso-Chaves, F. M. and Orozco, M.: El sistema de fallas extensionales en La Axarquía (Sierras de Tejeda y La Almijara, Cordilleras Béticas), Geogaceta, 24, 15–18, 1998.

Barrenechea, J. F., Rodas, M., Frey, M., Alonso-Azcarate, J., and Mas, J. R.: Chlorite, corrensite, and chlorite-mica in late Jurassic fluvio-lacustrine sediments of the Cameros basin of northeastern Spain, Clay Clay Miner., 48, 256–265, 2000.

Bourdelle, F.: Low-temperature chlorite geothermometry and related recent analytical advances: A review, Minerals, 11, 130, https://doi.org/10.3390/min11020130, 2021.

Bourdelle, F. and Cathelineau, M.: Low-temperature chlorite geothermometry: a graphical representation based on a T–R^{2+}–Si diagram, Eur. J. Mineral., 27, 617–626, https://doi.org/10.1127/ejm/2015/0027-2467, 2015.

Bourdelle, F., Parra, T., Chopin, C., and Beyssac, O.: A new chlorite geothermometer for diagenetic to low-grade metamorphic conditions, Contrib. Mineral. Petrol., 165, 723–735, https://doi.org/10.1007/s00410-012-0832-7, 2013.

Braga, J. C., Martín, J. M., and Quesada, C.: Patterns and average rates of late Neogene-Recent uplift of the Betic Cordillera, SE Spain, Geomorphology, 50, 3–26, 2003.

Cliff, G. and Lorimer, G. W.: The quantitative analysis of thin specimens, J. Microsc., 103, 203–207, https://doi.org/10.1111/j.1365-2818.1975.tb03895.x, 1975.

Cohen, K. M., Finney, P. L., Gibbard, P. L., and Fan, J. F.: The ICS International Chronostratigraphic Chart, Episodes, 36, 199–204, https://doi.org/10.18814/epiiugs/2013/v36i3/002, 2013.

Collettini, C., Niemejer, A., Viti, C., and Marone C.: Fault zone fabric and fault weakness, Nature, 462, 907–910, https://doi.org/10.1038/nature08585, 2009.

De Larouzière, F.D., Bolze, J., Bordet, P., Hernández, J., Montenat, C., and Ott d'Estevou, P.: The Betic segment of the lithospheric Trans-Alboran shear zone during the Late Miocene, Tectonophysics 152, 41–52, 1988.

Fulignati, P.: Hydrothermal alteration in epithermal and porphyry systems: Processes and products. In: Hydrothermal Mineral Deposits: Principles and Fundamental Concepts for the Exploration Geologist, Springer, 101–135, ISBN: 978-1-4020-8612-0, 2020.

Galindo-Zaldívar, J., Gil, A. J., Borque, M. J., González-Lodeiro, F., Jabaloy, A., Marín-Lechado, C., Ruano, P., and Sanz de Galdeano, C.: Active faulting in the internal zones of the central Betic Cordilleras (SE Spain), J. Geodyn., 36, 239–250, 2003.

Galindo-Zaldívar, J., Gil, A. J., Sanz de Galdeano, C., Shanov, S., Stanica, D.: Monitoring of active tectonic structures in Central Betic Cordillera (Southern Spain), Acta Geodyn. Geomater., 4, 19–29, 2007.

Galindo-Zaldívar, J., Gil, A. J., Sanz de Galdeano, C., Lacy, M. C., García-Armenteros, J. A., Ruano, P., Ruiz, A. M., Martínez-Martos, M., and Alfaro, P.: Active shallow extension in central and Eastern Betic Cordillera from CGPS data, Tectonophysics, 663, 290–401, https://doi.org/10.1016/j.tecto.2015.08.035, 2015.

Gil, A. J., Galindo-Zaldívar, J., Sanz de Galdeano, C., Borque, M.J., Sánchez-Alzola, A., Martínez-Martos, M., and Alfaro, P.: The Padul normal fault activity constrained by GPS data: Brittle extension orthogonal to folding in the central Betic Cordillera, Tectonophysics, 712/713, 64–71, https://doi.org/10.1016/j.tecto.2017.05.008, 2017.

Jiang, W. and Peacor, D.: Formation of corrensite, chlorite and chlorite-mica stacks by replacement of detrital biotite in low-grade pelitic rocks, J. Metamorph. Geol., 12, 867–884, 1994.

Jiménez-Millán, J., Velilla, N., and Vázquez, M.: Two-stage formation of kaolinite in shear-zone slates, southern Iberian Massif, SE Spain, Clay Miner., 42, 273–286, https://doi.org/10.1180/claymin.2007.042.3.01, 2007.

Jiménez-Millán, J., Abad, I., and Nieto, F.: Contrasting alteration processes in hydrothermal altered dolerites from the Betic Cordillera (Spain), Clay Miner., 43, 267–280, 2008.

Johnson, C.: Resolving denudational histories in orogenic belts with apatite fission-track thermochronology and structural data: An example from southern Spain, Geology, 25, 623–626, 1997.

Hürtgen, J., Rudersdorf, A., Grützner, C., and Reicherter, K.: Morphotectonics of the Padul-Nigüelas Fault Zone, southern Spain, Ann. Geophys., 56, S0679, https://doi.org/10.4401/ag-6208, 2013.

Inoue, A., Inoué, S., and Utada, M.: Application of chlorite thermometry to estimation of formation temperature and redox conditions, Clay Miner., 53, 143–158, 2018.

Lanari, P., Wagner, T., and Vidal, O.: A thermodynamic model for di-trioctahedral chlorite from experimental and natural data in the system MgO-FeO-Al_2O_3- SiO_2-H_2O: Applications to P-T sections and geothermometry, Contrib. Mineral. Petrol., 167, 968, https://doi.org/10.1007/s00410-014-0968-8, 2014.

Martín, J. M., Torres-Ruiz, J., and Fonboté, L.: Facies control of strata-bound ore deposits in carbonate rocks: the F-(Pb-Zn) deposits in the Alpine Triassic of the Alpujárrides, southern Spain, Mineral. Deposita, 22, 216–226, 1987.

McDonough, W. F. and Sun, S. S.: The composition of the Earth, Chem. Geol., 120, 223–253, https://doi.org/10.1016/0009-2541(94)00140-4, 1995.

Morales, J., Serrano, I., Vidal, F., and Torcal, F.: The depth of the earthquake activity in the Central Betics (Southern Spain), Geophys. Res. Lett., 24, 3289–3292, 1997.

Muñoz-Cemillán, A., Muñoz-Martín, A., Olaiz, A. J., and de Vicente, G.: Analysis of the geotermal potential on the Iberian Peninsula using magnetic spectral method and comparison with other data in different tectonic domains, J. Iber. Geol., 51, 581–596, https://doi.org/10.1007/s41513-025-00320-x, 2025.

Nieto, F., Mata, P., Bauluz, B., Giorgetti, G., Árkai, P., and Peacor, D. R.: Retrograde diagenesis, a widespread process on a regional scale, Clay Mineral., 40, 93–104, 2005.

Pouchou, J. L. and Pichoir, F.: Quantitative Analysis of Homogeneous or Stratified Microvolumes Applying the Model "PAP", in: Electron Probe Quantification, edited by: Heinrich, K. F. J. and Newbury, D. E., Plenum Press, New York, 31–75, https://doi.org/10.1007/978-1-4899-2617-3_4, 1991.

Rodríguez-Peces, M. J., García-Mayordomo, J., Azañón, J. M., and Jabaloy, A.: GIS application for regional assessment of seismically induced slope failure in the Sierra Nevada Range, South Spain, along the Padul Fault, Environ. Earth Sci., 72, 2423–2435, https://doi.org/10.1007/s12665-014-3151-7, 2014.

Rudersdorf, A., Hürtgen, J., Grützner, C., and Reicherter, K.: Neotectonic activity of the Granada Basin: new evidence from the Padul-Nigüelas Fault Zone, 2nd INQUA, 214–217, ISBN: 978-960-466-093-3, 2011.

Ruiz, A. M., Ferhat, G., Alfaro, P., Sanz de Galdeano, C., Lacy, M. C., Rodríguez-Caderot, G. and Gil, A. J.: Geodetic measurements of crustal deformation on NW-SE faults of the Betic Cordillera, southern Spain, 1999–2001, J. Geodyn., 35, 259–272, 2003.

Sanz de Galdeano, C.: Datos sobre las deformaciones neógenas y cuaternarias del sector del Padul. Reunión sobre la geodinámica de la Cordillera Bética y Mar de Alborán. Universidad de Granada, 1976.

Sanz de Galdeano, C.: Geologic evolution of the Betic Cordilleras in the Western Mediterranean, Miocene to present, Tectonophysics, 172, 107–119, https://doi.org/10.1016/0040-1951(90)90062-D, 1990.

Sanz de Galdeano, C.: La Cordillera Bética, Editorial Punto Rojo Libros, Sevilla, 116 pp., ISBN 9788419093417, 2022.

Sanz de Galdeano, C. and Alfaro, P.: Tectonic significance of the present relief of the Betic Cordillera, Geomorphology, 63, 175–190, https://doi.org/10.1016/j.geomorph.2004.04.002, 2004.

Sanz de Galdeano, C. and López-Garrido, A. C.: Estratigrafía y estructura de las unidades alpujárrides en el borde occidental de Sierra Nevada (Granada, España), Rev. Soc. Geol. Esp., 12, 187–198, 1999.

Sanz de Galdeano, C. and López-Garrido, A. C.: Revisión de las Unidades Alpujárrides de las Sierras de Tejeda, Almijara y Guájares (Sector Central de la Zone Internal Bética, Provincias de Granada y Málaga), Rev. Soc. Geol. Esp., 16, 135–149, 2003.

Sanz de Galdeano, C., García-Tortosa, F. J., Peláez, J. A., Alfaro, P., Azañón, J. M., Galindo-Zaldívar, J., López-Casado, C., López-Garrido, A. C., Rodríguez-Fernández, J., and Ruano, P.: Main active faults in the Granada and Guadix-Baza basins (Betic Cordillera), J. Iber. Geol., 38, 209–223, https://doi.org/10.5209/rev_JIGE.2012.v38.n1.39215, 2012.

Simancas, J. F. and Campos, J.: Compresión NNW-SSE tardi a postmetamórfica, y extensión subordinada, en el Complejo Alpujárride (Dominio de Alborán, Orógeno Bético), Rev. Soc. Geol. Esp., 6, 23–35, 1993.

Smeraglia, L., Billi, A., Carminati, E., Cavallo, A., Di Toro, G., Spagnuolo, E., and Zorzi, F.: Ultra-thin clay layers facilitate seismic slip in carbonate faults, Sci. Rep. 7, 664, https://doi.org/10.1038/s41598-017-00717-4, 2017.

Stich, D., Morales. J., López-Comino. J.A., Araque-Pérez, C., Azañón, J. M., Dengra, M. A., Ruiz, M., and Weber, M.: Seismogenic structures and active creep in the Granada Basin (S-Spain), Tectonopysics, 882, 230368, https://doi.org/10.1016/j.tecto.2024.230368, 2024.

Taylor, S. R. and McLennan, S. M.: The continental crust: its composition and evolution, Blackwell, Oxford, 1985.

Tubía, J. M., Cuevas, J., Navarro-Vilá, F., Álvarez, F., and Aldaya, F.: Tectonic evolution of the Alpujarride Complex (Betic Cordillera, southern Spain), J. Struct. Geol., 14, 193–203, 1992.

Verdecchia, S., Collo, G., Zandomeni, P. S., Wunderlin, C., and Fehrmann, M.: Crystallochemical indexes and geothermobarometric calculations as a multiproxy approach to P-T condition of the low-grade metamorphism: The case of the San Luis Formation, Eastern Sierras Pampeanas of Argentina, Lithos, 324/325, 385–401, https://doi.org/10.1016/j.lithos.2018.11.021, 2019.

Vidal, O., Lanari, P., Munoz, M. Bourdelle, F., and de Andrade, V.: Deciphering temperature, pressure and oxygen-activity conditions of chlorite formation, Clay Miner., 51, 615–633, https://doi.org/10.1180/claymin.2016.051.4.06, 2016.

Warr, L. N.: IMA-CNMNC approved mineral symbols, Miner. Mag., 85, 291–320, https://doi.org/10.1180/mgm.2021.43, 2021.

Wiewiora, A. and Weiss, Z.: Crystallochemical classifications of phyllosilicates based on the unified system of projection of chemical composition; II, The Chlorite Group, Clay Miner., 25, 83–92, https://doi.org/10.1180/claymin.1990.025.1.09, 1990.

Wintsch, R. P., Christoffersen, R., and Kronenberg, A. K.: Fluid-rock reaction weakening of fault zones, J. Geophys. Res.-Sol. Ea., 100, 13021–13032, https://doi.org/10.1029/94JB02622, 1995.

Xu, Z., Yu, T., Lin, P., and Li, S.: Anomalous patterns of clay minerals in fault zone, Eng. Geol., 325, 107279, https://doi.org/10.1016/j.enggeo.2023.107279, 2023.